Detection of the yellow-leaf disease of rubber trees using low-altitude digital imagery from UAV

Jiangtao Qi[1,2*], Mao Li[1,2], Huiming Zhang[3*], Tiwei Zeng[4]

(1. *Key Laboratory of Bionic Engineering, Ministry of Education, Jilin University, Changchun 130000, China*;
2. *College of Biological and Agricultural Engineering, Jilin University, Changchun 130000, China*;
3. *Mechanical and Electrical Engineering College, Hainan University. Haikou 570100, China*;
4. *School of Information and Communication Engineering, Hainan University. Haikou 570100, China*)

Abstract: Efficient and non-destructive detection of rubber tree diseases is of great significance for optimizing disease control measures for pesticide application and fertilization. In this study, the feasibility of rubber yellow-leaf disease monitoring based on a low-altitude unmanned aerial vehicle (UAV) remote sensing platform was explored, and a low-cost method for detecting yellow-leaf disease based on visible light sensors was proposed. We compared the difference between the spectral response of each band of the visible light sensor in the diseased area and the healthy area, and then decorrelated and stretched the image in the RGB color space, thereby enhancing the color separation between highly correlated channels and enhancing the color difference of the image. Then we converted the image to the HSV color space, comparing the detection effect of different morphological parameters on yellow-leaf diseases and optimizing the extraction of the diseased area. The experimental results showed that this study provides the distribution information of yellow-leaf disease of rubber trees, and the R^2 of the regression model of rubber trees was greater than 0.8. This study holds significance for optimizing disease control and sustainable development of the rubber industry.

Keywords: rubber tree, yellow-leaf disease, low-altitude digital imagery, UAV
DOI: 10.25165/j.ijabe.20241706.9213

Citation: Qi J T, Li M, Zhang H M, Zeng T W. Detection of the yellow-leaf disease of rubber trees using low-altitude digital imagery from UAV. Int J Agric & Biol Eng, 2024; 17(6): 245–255.

1 Introduction

Natural rubber plays a crucial role in the development of the national economy, modern industry, and national defense. It not only supplies essential rubber products for daily use, medical purposes, and light industries, but also provides rubber components for machinery manufacturing, the automobile industry, national defense, and aerospace industries[1-3]. As a valuable resource with limited availability, natural rubber possesses unique characteristics that make it essential in the production and performance of various products. This has solidified the strategic position of the global natural rubber industry. In addition, due to many factors such as global warming, continuous cropping challenges, and irreversible ecological damage caused by human activities, new rubber diseases have emerged. Therefore, the monitoring, prevention, and control of natural rubber diseases have become one of the important ways for the sustainable development of the rubber industry[4-8].

Rubber trees are tall, growing to a height of up to 43 m in the wild[9]. They require specialized monitoring and early warning for diseases and pests. This work demands a high level of professionalism and scientific knowledge. The effectiveness of the monitoring technology directly affects the reliability of the results and the workload of those conducting the monitoring. At present, pest monitoring of natural rubber mainly relies on manual surveys for forecasting. For a long time, the concept of emphasizing treatment and neglecting prevention has not fundamentally changed. Disaster relief after severe disasters and pre-disaster defense has led to the failure to take preventive and countermeasures when some rubber tree diseases and insect pests break out, often causing large economic losses and destroying the ecological balance of the rubber forest system[10,11]. Therefore, there is an urgent need to adopt modern advanced technology to replace traditional manual investigation.

To address these challenges, researchers have been exploring new technologies and approaches for detecting and monitoring rubber tree diseases. Hyperspectral reflectance data (350-2500 nm) of healthy and powdery mildew-infected leaves were measured and classified in the laboratory using a spectroradiometer by Cheng et al.[12] Kaewboonma et al.[13] used currently popular deep learning algorithms in the lab to detect individual rubber leaves with the disease. Deep learning algorithms are popular in the field of detecting leaf diseases. Li et al.[14] proposed the EfficientNet-B1 model for detecting tea diseases and developed a mini program. Yin et al.[15] proposed a simple and effective method to improve the accuracy of grape leaf disease recognition based on deep transfer learning and an improved MobileNetV3 model (GLD-TTL). Lang et al.[16] fused hyperspectral and deep learning techniques to rapidly evaluate wheat resistance to Fusarium head blight. However, these studies were only conducted in the laboratory and cannot achieve large-scale disease detection.

Received date: 2023-11-15 **Accepted date:** 2024-09-10
Biographies: Mao Li, PhD candidate, research interest: precision agriculture and intelligent agricultural machinery, Email: limao234@163.com; **Tiwei Zeng**, PhD candidate, research interest: intelligent agricultural machinery equipment, Email: 20081000110018@hainanu.edu.cn.

***Corresponding author: Jiangtao Qi**, PhD, Professor, research interest: precision agriculture and intelligent agricultural machinery. College of Biological and Agricultural Engineering, Jilin University, Changchun 130000, China. Tel: +86-15164355463, Email: qijiangtao@jlu.edu.cn; **Huiming Zhang**, PhD, research interest: design of agricultural machinery, Mechanical and Electrical Engineering College, Hainan University. Haikou 570100, China. Tel: +86-18608973300, Email: 914860430@qq.com.

Remote sensing technology has played a crucial role in crop management. It involves analyzing the spectrum of energy absorbed, reflected, and transmitted by plants to improve the input efficiency of agronomic practices, i.e. fertilizer, irrigation, and pesticides. With the miniaturization of image sensors and the development of low-altitude drones, especially small commercially available drones, unmanned aerial vehicles (UAVs) have begun to be seen as a potential remote sensing platform because of their ability to provide higher spatial resolution and time-sensitive results[17-19]. The technological advancements in producing digital images and extracting meaningful information from images provide the potential for automation to replace traditional manual investigation[20,21]. Tao et al.[22] combined UAV and spectroscopic techniques to conduct a comprehensive survey of breeding populations of slash pine at two sites to monitor spectral bands, vegetation indices (VIs), and tree growth characteristics. Based on the UAV remote sensing method, Zhou et al.[23] used image processing methods to estimate the coverage of surface crop residues in farmland. Rastogi et al.[24] proposed a semi-automatic image segmentation algorithm for plant leaf diseases to distinguish between diseased areas and disease-free areas in leaves, but the algorithm is only for leaf disease identification under an artificial background, and cannot achieve real-time detection and recognition. Wspanialy et al.[25] proposed a model for crop leaf disease type detection and disease severity detection for public datasets. The model uses a 50-layer residual network (ResNet-50) to classify diseases, and the U-net network assesses the severity of the disease. Liu et al.[26] used hyperspectral sensors to obtain remote sensing images of wheat scabs in the field, and combined them with BP neural networks to identify wheat scabs. Deng et al.[27] screened and evaluated 30 different VIs and their optimal band combinations based on airborne hyperspectral data of wheat stripe rust, to quantitatively assess wheat stripe rust disease. Gao et al.[28] proposed a corn disease detection method based on an improved MobileNet V3 small, which uses drones to collect corn disease images and applies MobileNet V3 small to detect corn diseases. Wang et al.[29] tested the effectiveness of the band optimization method for UAV hyperspectral images using RF and GBDT models, and obtained an effective hyperspectral feature band selection method and a model approach for high-precision monitoring of rice blast disease. Li et al.[30] collected hyperspectral drone data in southeast China and used linear discriminant analysis (LDA) to determine the separability of healthy trees and trees at an early stage of infection. In addition, drones can carry a variety of sensors to estimate chlorophyll content and nitrogen deficiency symptoms in crop leaves[31-33]. However, the high cost of hyperspectral imaging devices carried by drones makes it difficult to promote their widespread application. Currently, there is no research on using low-cost visible light images for monitoring rubber tree diseases.

A major disease affecting rubber trees is yellow-leaf disease. Yellow-leaf disease occurs due to the lack of nutrients nitrogen, potassium, and magnesium throughout the plant's growth process. In addition, yellow leaves are produced by infectious diseases[34]. Yellow-leaf disease will affect the growth of rubber trees, impede photosynthesis, and reduce rubber production. The more serious impact is that the whole rubber tree will turn yellow, and the tree will become weak until death. Due to the high height of rubber trees, it is difficult to assess the disease situation by manpower alone at present.

In past research work, rubber-using UAVs have been rare. Hamid et al.[35] mapped the NDVI of rubber plantations, and the overall results showed that the trees in the rubber plantations were generally healthy, so the study is not very representative. However, there is not any disease monitoring research for rubber trees utilizing inexpensive and visible light images at this time. To the best of our knowledge, this study is the first to report a study using visible light images to monitor rubber tree diseases.

dThis study aimed to detect yellow-leaf disease in rubber trees by using low-altitude remote sensing images obtained by UAV platforms. The potential of this research will benefit rubber tree growers who will be able to adopt this technology to achieve rapid and large-scale yellow-leaf disease monitoring in their rubber growing areas. Yellow-leaf disease causes changes in the appearance of the infected rubber tree canopy, such as yellowing and wilting of the leaves, which in turn affects the color and morphological characteristics of the rubber tree canopy in drone images. Considering the low cost of visible light image sensors, this study explored the feasibility of rubber yellow-leaf disease monitoring based on a low-altitude UAV visible light remote sensing platform. We monitored the situation of yellow-leaf disease by monitoring the yellow condition of the canopy. We analyzed and compared the differences in the spectral response of each band of visible light sensor in the diseased area and the healthy area, and decorrelated and stretched the image in the RGB color space, thereby enhancing the color separation between highly correlated channels and enhancing the color difference of the image. Then, the image was converted to the HSV color space, the detection effect of the parameters of different morphological algorithms on yellow-leaf diseases was compared, and the extraction of the diseased area was optimized (Figure 1).

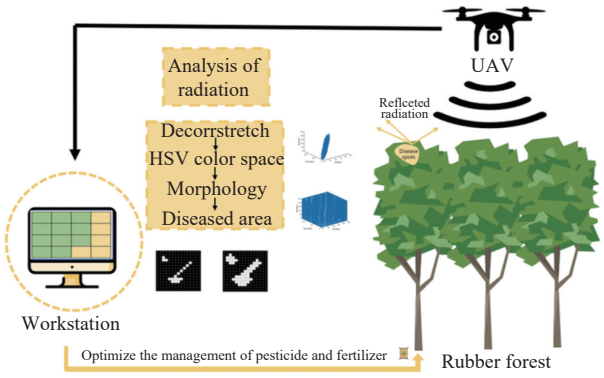

Figure 1 Research content and significance

2 Materials and methods

2.1 Study area and drone image collection

The experimental site of this study is located in Danzhou City, Hainan Province, China. Its geographic coordinates are 109°28′44″E and 19°31′42′′N. It has a tropical monsoon island climate with an average annual temperature of 23.9°C. The highest temperature is in July and the lowest temperature is in January. The average annual precipitation is 1721.6 mm, and the rainy season lasts from May to October each year. Rubber is the leading industry in the local area. The rubber trees planted at this experimental site were 6 years old and of the variety Reyan 7-33-97 (*Hevea brasiliensis*, Reyan 7-33-97), which has a fast growth rate and excellent characteristics of strong resistance, great glue production potential, and good physical and chemical properties of dry glue[36,37]. There were a total of 1693 rubber trees, divided into healthy and infected trees. Although there were various degrees of yellow-leaf diseases, this study categorized

them into a single group of infections. According to the field survey results, there were 921 healthy rubber trees and 772 infected trees. Figure 2 shows the location of the experimental site.

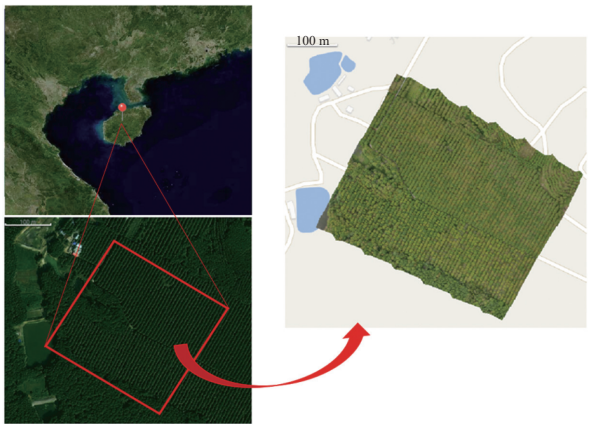

Figure 2 Location of the study areas

Drone images were collected on May 3 and 8, 2021. The experimental site covers an area of about 15 hm^2, and the drone used in the experiment is DJI's Phantom 4 multispectral drone equipped with a 2M pixel RGB camera. This study used only images in the visible light band. The camera exposure time was automatically matched to the ambient conditions. The UAV maintained an altitude of 50 m from the ground, a flight speed of 3 m/s, a camera trigger frequency of 0.8 s, a forward overlap rate of 80%, and a side overlap rate of 70%. The spatial resolution (GSD) of the image was 4 cm. The drone used the D-RTK 2 high-precision GNSS mobile station to acquire real-time differential data and collect the exact coordinates of the target point (Figure 3). Finally, 231 images of rubber trees were obtained.

Figure 3 D-RTK 2 high-precision GNSS mobile station

2.2 Rubber crown division

In this study, the simple linear iterative cluster (SLIC) superpixel method[38] was used to segment and extract canopy samples from the rubber canopy in the acquired images. The SLIC algorithm was chosen because it uses *K*-means clustering to efficiently generate a series of small regions-superpixels-of pixels that are located next to each other and have similar characteristics such as color, luminance texture, etc. The SLIC algorithm is fast and memory efficient. The sample extraction process of the rubber trees canopy superpixel block is shown in Figure 4. First, the UAV captured images of the rubber tree canopy. Then, the SLIC algorithm was applied to process the image and generate superpixel blocks. Lastly, three individuals with expertise classified the pixel blocks and obtained samples.

a. Image acquisition b. SLIC segmention c. Samples

Note: SLIC: Simple linear iterative cluster.

Figure 4 Workflow of SLIC segmentation

To obtain samples, the image acquired by the drone was segmented according to the parameters (*K* and sigma, etc.) using the SLIC algorithm. The segmentation of individual rubber trees can be adjusted by three parameters: *K*, sigma, and *n*_segments. In this study, *K* was set to 2000 to divide the plantation image into 2000 superpixel segments, which corresponded to an average size for segmenting the leaf area. A sigma value of 10 was chosen to ensure the compactness limit of the superpixel segments adhered to the SLIC algorithm.

The dimensions of each image were 1600×1300 pixels, for a total of 2 080 000 pixels. Each image contained about 110 rubber trees and had centimeter-level positioning coordinates. DJI Terra was used to reconstruct large fields covering thousands of rubber trees, ensuring the adaptability of this approach. Therefore, the segmentation parameter *n*_segments could be determined to be 110. In addition, the canopy image of rubber trees obtained by UAV revealed that the crown size did not change significantly after it was infected with yellow-leaf disease, which may be because the disease was not very serious when the UAV flew. Therefore, the same parameters *K*, sigma, and *n*_segments were maintained in this study. In the end, 3043 superpixel blocks were produced.

2.3 HSV color model and decorrstretch

The digital image was stored in the computer in the form of a matrix, and the color image was usually stored in the RGB format. The color digital image is a three-dimensional matrix, in which the first dimension matrix is the red component (*R*), the second dimension matrix is the green component (*G*), and the third dimension matrix is the blue component (*B*). The value of each dimension element in the matrix ranges from 0 to 255. In the computer system, 8-bit bytes represent an element value, each dimension can represent 2^8 kinds of color levels, and the three dimensions can represent 2^{24} kinds of colors in total. The number of colors that human eyes can roughly distinguish is relative to this, so the color image formed by RGB is usually called true color. Since

R, *G*, and *B* components of object color in digital images are all related to the amount of light irradiated on the object, all three components of an image obtained in darkness are low, and all three components of an image obtained in full sunlight are high, so the three color components of an RGB image are positively correlated with brightness, which is not conducive to processing and analysis of the image.

In contrast, the HSV model has its unique advantages in image processing. The hue component *H*, saturation component *S*, and brightness component *V* are independent of each other. Secondly, the HSV model is more intuitive than the RGB model to show the hue, vividness, and brightness of the color, which is more consistent with the perception of color by human eyes. Therefore, this study converted RGB images into HSV color space for subsequent processing.

As shown in Figure 5, any point within the cone corresponds to a color. The central angle of the bottom side represents the hue *H*, which ranges from 0° to 360°. The value is calculated counterclockwise from red, which is 0° for red, 120° for green, and 240° for blue. The distance between a point on the bottom and the center of the circle represents the saturation *S*. The higher the saturation, the darker and brighter the color. The value range of *S* is 0%-100%. The vertical distance of a point in the cone to the bottom indicates lightness *V*, which indicates how bright the color is and ranges from 0% to 100% (black to white).

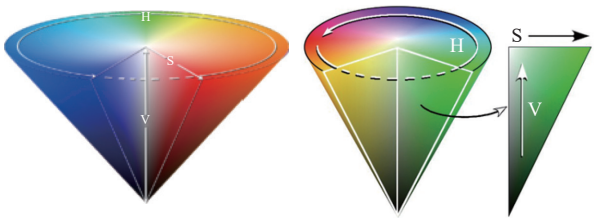

Figure 5 HSV color space

RGB image to HSV image:

$$R = \frac{R}{255} \tag{1}$$

$$G = \frac{G}{255} \tag{2}$$

$$B = \frac{B}{255} \tag{3}$$

$$V = \max(R, G, B) \tag{4}$$

$$S = \begin{cases} \dfrac{V - \min(R,G,B)}{V} & if\ V \neq 0 \\ 0 \end{cases} \tag{5}$$

$$H = f(x) = \begin{cases} \dfrac{60 \times (G-B)}{V - \min(R,G,B)} & if\ V = R \\ \dfrac{120 + 60 \times (B-R)}{V - \min(R,G,B)} & if\ V = G \\ \dfrac{240 + 60 \times (R-G)}{V - \min(R,G,B)} & if\ V = B \end{cases} \tag{6}$$

where, *R*, *G*, and *B* respectively represent the Digital Number (DN) values of image Red (*R*), Green (*G*), and Blue (*B*) channels. *F*(*x*) represents the value of color hue, which ranges from 0° to 360°. *f*(*x*) represents the value of color tone, and its range is in 0°-360°.

If the calculated *H* value is less than 0, add 360 to the value to get the final *H* value:

$$H = H + 360 \tag{7}$$

where, *H* represents the hue value of images.

Since OpenCV needs to do the visualization of HSV images, it is finally necessary to convert each value to between 0-255:

$$H = \frac{H}{2} \tag{8}$$

$$S = S \times 255 \tag{9}$$

$$V = V \times 255 \tag{10}$$

where, *H* represents hue value, *S* represents saturation, and *V* represents lightness.

Images can be correlated to adapt to contrast through MATLAB's (MathWorks, Natick, MA, USA) decorrstretch function. This feature highlights diseased areas by enhancing plot color differences. MATLAB provides a variety of settable parameters for decorrelated stretching. *S*=decorrstretch(A, 'Tol', 0.01) applies decorrelation stretch to a multichannel image, where *S* is the image to be enhanced, specified as an RGB image; Tol is the degree of stretch to perform a linear contrast stretch after a decorrelation stretch, since the pixel grayscale value must be at [0, 255]; and 0.01 is the value of specific linear contrast stretching.

2.4 Grayscale-based method

The grayscale method is a widely used technique in digital image processing. It is used to convert color images into grayscale images. By converting images to grayscale, we can enhance visual contrast, highlight specific areas of interest, and facilitate the extraction of the rubber tree canopy area affected by yellow-leaf disease. Additionally, grayscale images have a lower dimension compared to color images, resulting in reduced memory usage and making image processing more convenient. Some common methods for graying images include the visual formula, decolorization formula, and lightness formula.

Visual formula:

$$\text{Gray}(i,j) = 0.299R(i,j) + 0.587G(i,j) + 0.114B(i,j) \tag{11}$$

$$R(i,j) = G(i,j) = B(i,j) = \text{Gray}(i,j) \tag{12}$$

As the human eye has different sensitivities to different colors (i.e., different wavelengths of light), the human eye is most sensitive to green light and less sensitive to blue and red light. The above formula, which weights the three RGB channels of color to obtain a grayscale image, reflects this physiological characteristic of the human eye and is a reasonable formula for graying, and is also the most classic grayscale formula. Python's grayscale function convert ('*L*') and the MATLAB library function rgb2gray principle are based on visual formulas.

Desaturation formula:

$$\text{Gray}(i,j) = \frac{[\max(R(i,j), G(i,j), B(i,j)) + \min(R(i,j) + G(i,j) + B(i,j))]}{2} \tag{13}$$

$$R(i,j) = G(i,j) = B(i,j) = \text{Gray}(i,j) \tag{14}$$

The desaturation formula is a grayscale formula that takes into account the contrast information of the image, which can better highlight the color contrast, and will be more obvious in some images with closer colors. Its algorithm is relatively simple: find the maximum and minimum values of the RGB three-channel value of each pixel, then calculate the mean of the two, and use the mean as the grayscale result. The desaturation formula is the principle of the

"Desaturate" function of the image processing software Photoshop.

Lightness formula:

$$\text{Gray}(i,j)=\frac{[R(i,j)+G(i,j)+B(i,j)]}{3} \tag{15}$$

$$R(i,j)=G(i,j)=B(i,j)=\text{Gray}(i,j) \tag{16}$$

The lightness formula is actually to take the red, green, and blue three-channel average of a pixel, and use the average value as the gray value of the pixel to achieve the grayscale effect.

2.5 Creation of color histograms

Color feature is a global feature based on image pixel. Color histogram is a widely used color feature. Color histogram quantitatively describes the statistical distribution of color in an image. Swain et al.[39] point out that color histograms are not sensitive to image geometric transformation (image rotation, translation, scaling, etc.) and image quality change (blur, etc.). This property makes the color histogram more suitable for the interpretation of global color-similar image features.

Each RGB image can be divided into three component grayscale images, and so correspondingly can be created as three histograms: a red component histogram, a green component channel histogram, and a blue component histogram. The horizontal axis of the histogram ranges from 0 to 255, representing the brightness of the corresponding color, where a value of 0 is all black, and 255 is the brightest white. The vertical axis represents the number of pixels at a certain level of brightness. Creating a color histogram helps to get more information from the image[40,41].

2.6 Morphological algorithms

Some of the sparse diseased canopies correspond to pixels that are also sparse, and the morphological dilation method used in this paper fills the gaps between the leaves, which can minimize the difference between the number of diseased rubbers counted manually and by image processing. In this study, fill was performed by the dilation command, J=imdilate(I, SE) for expanding grayscale, binary, or compressed binary image I, returning the expanded image J. SE is an array of structure element objects or structure element objects, returned by the strel or offsetstrel function.

Morphological dilation makes objects more visible and fills in small holes in objects. Lines appear thicker, and filled shapes appear larger. Morphological transformation dilation combines two sets using vector addition (or Minkowski set addition, such as $(a,b)+(c,d)=(a+c, b+d)$). The result of the operation $A \oplus B$ is the set of all possible combinations of vectors obtained by adding vectors from A and B.

$$A \oplus B=\left\{p \in \varepsilon^2,\ p=x+b,\ x \in A,\ b \in B\right\} \tag{17}$$

where A represents the original image; B represents the structure of the expansion element; and p represents the dilated image.

The dilation operation is an incremental operation, and when a dilation operation is performed on a binary image, only the processing of the boundary has an effect on the final result. The process of the dilation operation is as follows:

Initial set A and structure B (Figure 6).

Invert structure element B along the origin of structure element B, because structure element B is symmetric with respect to the origin, so the inverted is consistent with the uninverted.

The translation reverses the origin of the structural element B to the origin of the set A (the upper left corner of A) (Figure 7).

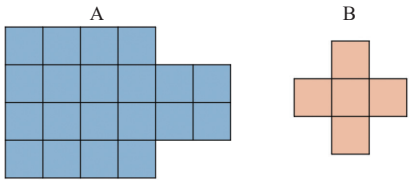

Figure 6 Initial set A and structure B

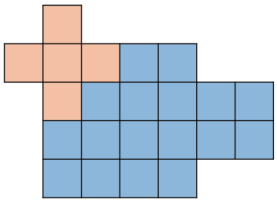

Figure 7 Origin of structural element B to origin of set A

Translate the inverted structure B of z, and find that the intersection of the inverted structure B and the set A after the first translation z is not empty (Figure 8).

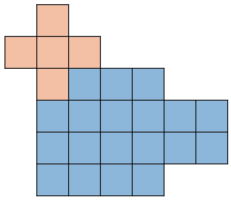

Figure 8 The intersection of B and set A is not empty

The z of the same translation is referenced to the origin, so it is the red position as shown in Figure 9.

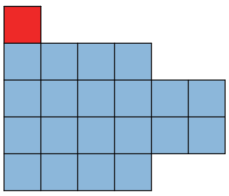

Figure 9 Original set image A and structural element Z before computation

Until all translations z are found that the intersection of the inverted structure element B with the set A is not empty. Get the result as shown below (Figure 10).

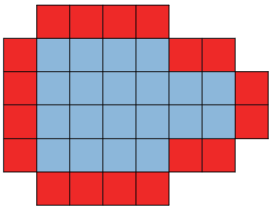

Figure 10 Expansion results

Among these, both blue and red represent the location resulting from the dilation after being processed by the inverted structural element B. The red represents the additional location after dilation, while the blue represents the original set A location. In other words, blue represents the dilated boundary of set A by one circle, which corresponds to the point that can be relatively close to the isolated point in the image operation.

2.7 Data analysis

The analysis of color information from RGB remote sensing images is of great importance for rubber tree yellow-leaf disease

monitoring. Due to changes in the structure and physicochemical properties of the rubber tree canopy caused by yellow-leaf infection, there are differences in the color information of the rubber canopy of healthy rubber trees and those with yellow-leaf disease. The color features used in this study included color coordinate values (*R*, *G*, *B*) and color-luminance-saturation (HSV) color space values derived from RGB images.

The RGB image data obtained by UAV was processed; this process is described in the previous sections. Firstly, the DN values of *R*, *G*, and *B* channels of rubber tree canopy images obtained by UAV were extracted, and the spectral responses of different bands of visible light sensors in the lesion area and healthy area were analyzed and compared. Then we enlarged the data difference of DN value, converted it into gray image, and tried to use a threshold to obtain the lesion area, but this method was not effective.

Subsequently, the image was decorrelated and stretched in the RGB color space, and the color separation between highly correlated channels was enhanced to enhance the color difference of the image. Then, the image was converted to the HSV color space, the diseased area was extracted through the threshold (Figure 11), and regression analysis was carried out to analyze the ability of UAV-derived lesion area pixels to predict the number of diseased rubber trees.

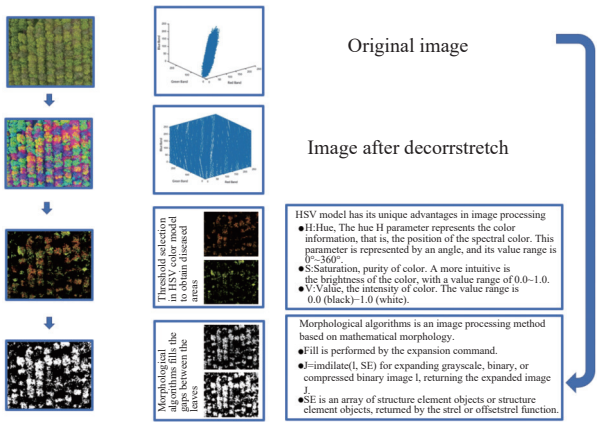

Figure 11 Flowchart of the theoretical image processing steps

3 Results and discussion

3.1 Attention mechanism comparison results

3.1.1 Analysis of radiation

As shown in Figure 12, the superpixel color features of yellow-leaf disease infection and healthy rubber trees were extracted. Figure 12 presents the statistical information of DN values for both healthy and diseased rubber tree canopy sample images.

By analyzing this statistical information, the contrast between the DN values of healthy and diseased areas can be enhanced, allowing us to accurately extract the diseased regions. Due to changes in the structure and physicochemical properties of rubber canopy caused by yellow-leaf infection, significant differences in the DN value of healthy rubber trees and those infected with yellow-leaf disease can be observed. As shown in Figure 12, the DN values of the three channels of rubber tree canopy *R*, *G*, and *B* with yellow-leaf disease were lower than those of healthy rubber trees. Further analysis revealed that the difference in DN value was most pronounced in the *R* channel. The median DN value of the rubber tree *R* channel with yellow-leaf disease was higher than the median DN value of the healthy rubber tree *R* channel is more than 20.

3.1.2 Different grayscale methods

Binarization of an image is to set the grayscale value of the pixels on the image to 0 or 255, showing the entire image in obvious black and white, that is, dividing the image into two parts: background and foreground. Image binarization can extract areas of diseased rubber trees. Image binarization first requires converting a color image to a grayscale image, and then determining the binarization boundaries (thresholds) of the background and foreground to complete the binarization. At present, there are three commonly used algorithms for color image grayscale: lightness formula, visual formula, and color removal formula. In this study, the *R* channel with the largest difference was extracted separately, and the gray value of the *R* channel was expanded by 1.8 times (Figure 13).

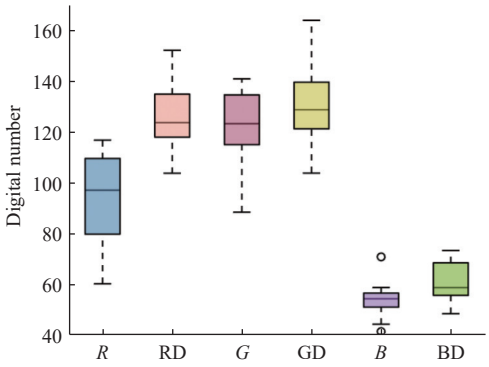

Note: *R* represents the DN value of the red channel in a healthy rubber tree crown image; RD represents the DN value of the red channel in a rubber tree crown image with yellow-leaf disease; *G* represents the DN value of the green channel in a healthy rubber tree crown image; GD represents the DN value of the green channel in a rubber tree crown image with yellow-leaf disease; *B* represents the DN value of the blue channel in a healthy rubber tree crown image; and BD represents the DN value of the blue channel in a rubber tree crown image with yellow-leaf disease.

Figure 12 Distribution of DN values of each color channel in areas with yellow-leaf disease and healthy rubber

This maximizes the gray value of the vast majority of diseased rubber trees and maximizes the difference in DN values. In this study, the three commonly used grayscale methods were also used to grayscale the rubber tree images of drones (Figure 14).

3.1.3 Disease estimation

Three seasoned experts were assigned the task of tallying the quantity of diseased rubber trees in the UAV image. Their observations were later compared to the counting results foreseen by the algorithm through regression analysis. Using the “bwlabel” function to count the pixel clusters, the number of pixel clusters was considered the number of diseased rubber trees. In the image of RGB color space, the number of diseased rubber trees obtained after image segmentation was less correlated with the number of manual observations, the lightness formula, the decolorization formula, and the visual formula grayscale, and the number of counts after image segmentation was less than 0.1. This study analyzed the information of the *R*, *G*, and *B* channels of superpixel blocks of yellow-leaf disease rubber trees, and expanded the color difference. The correlation was the highest among the four grayscale methods (R^2=0.18), indicating that numerical detection of yellow-leaf disease rubber trees by threshold segmentation within the RGB color space is not feasible (Figure 15).

RGB is suitable for display systems, but not for image segmentation and analysis. The RGB color space uses a linear combination of the three color components to represent colors, so

a. Original images

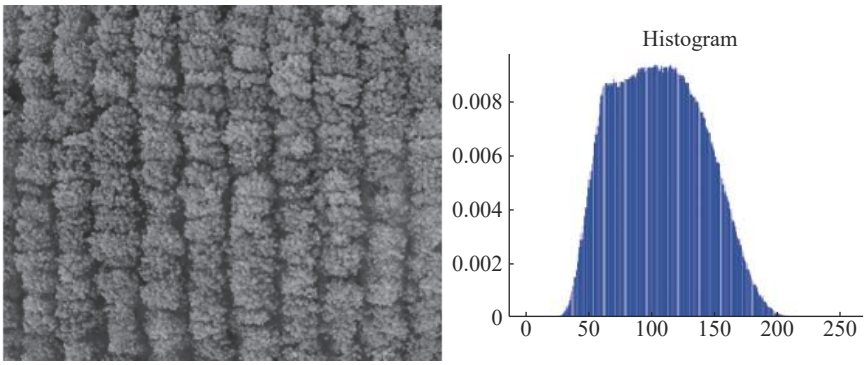

b. Histogram corresponding to the grayscale diagram obtained by the visual formula and the grayscale diagram

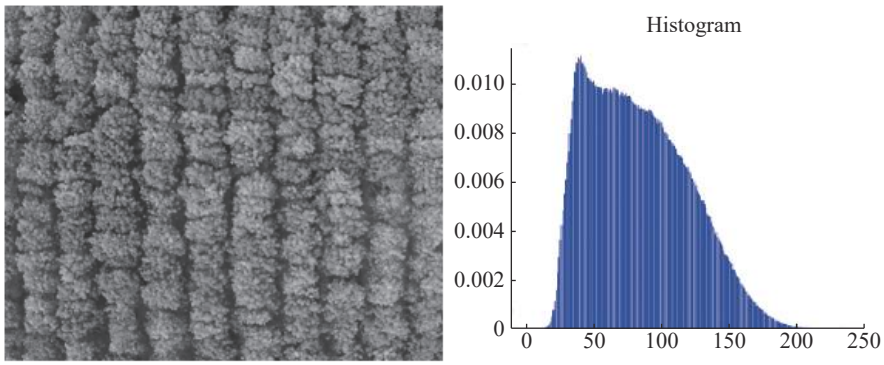

c. Histogram corresponding to the grayscale diagram obtained by the visual formula and the grayscale diagram

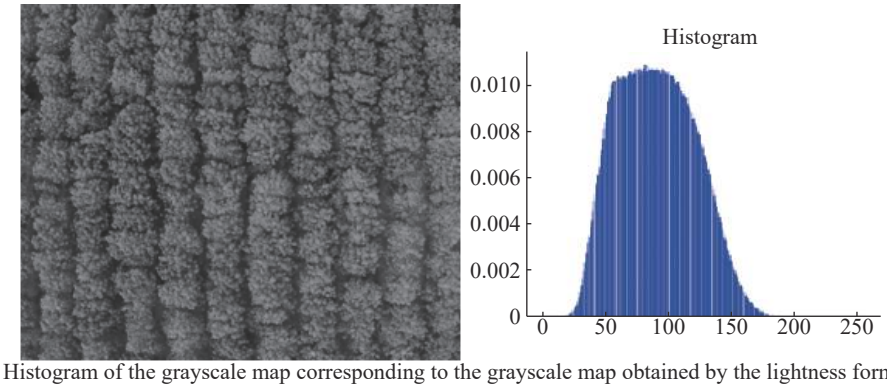

d. Histogram of the grayscale map corresponding to the grayscale map obtained by the lightness formula

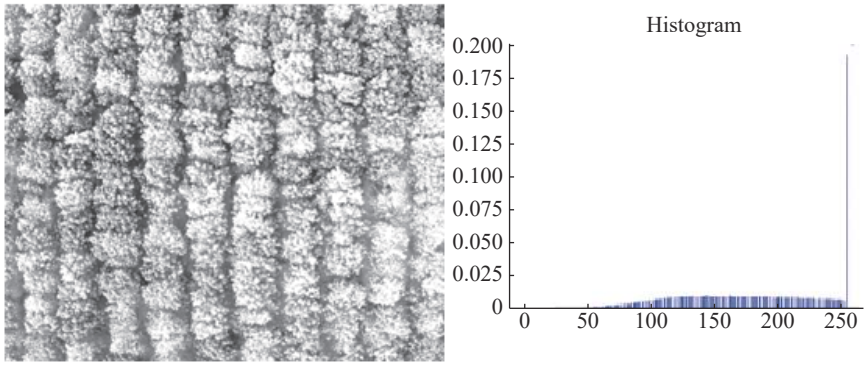

e. Histogram of the grayscale diagram and the grayscale diagram obtained by this research method

Figure 13 Grayscale results

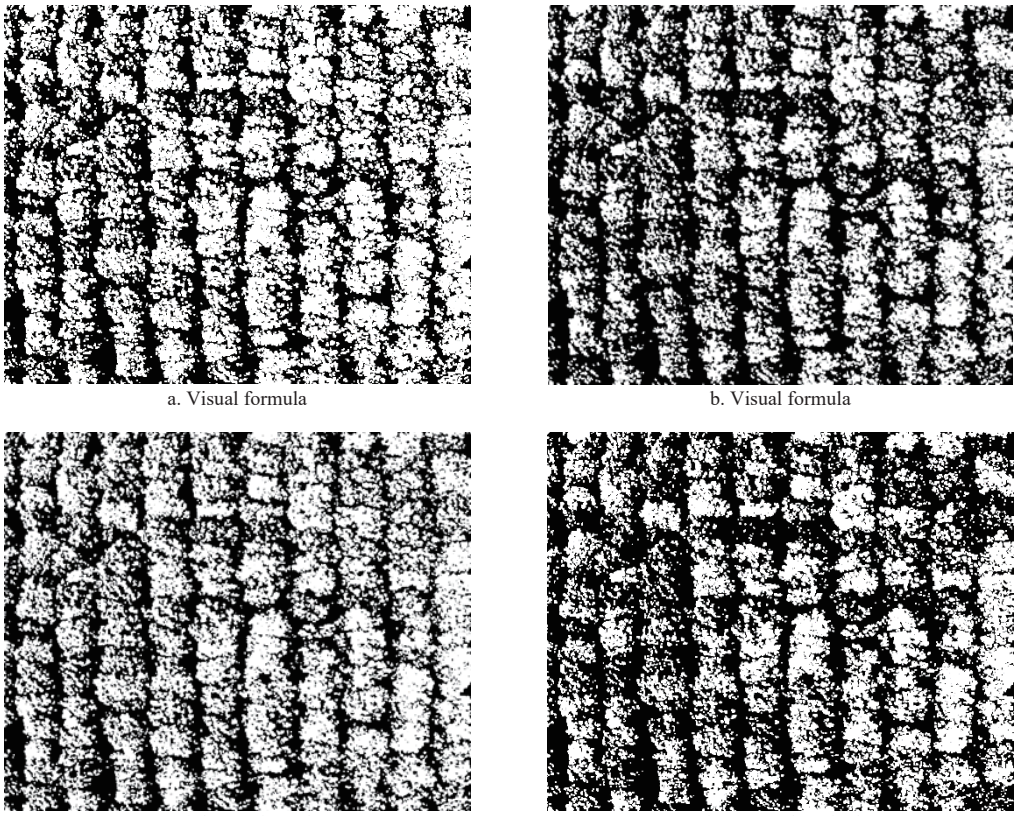

a. Visual formula b. Visual formula

c. Lightness formula d. Proposed method

Figure 14 Binary plot obtained after threshold segmentation

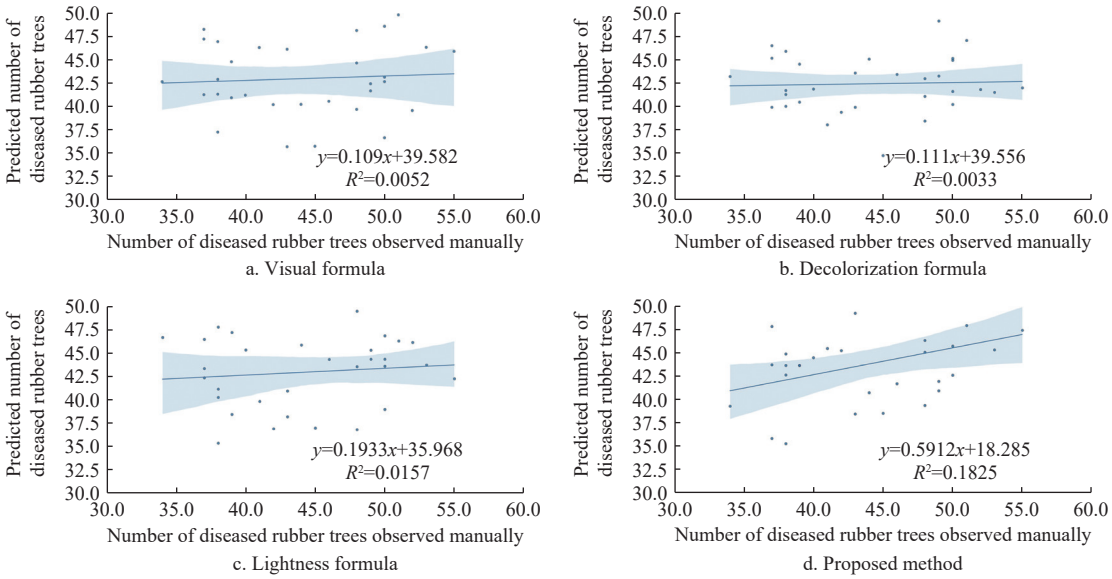

a. Visual formula b. Decolorization formula

c. Lightness formula d. Proposed method

Figure 15 Correlation between the percentage (%) of yellow pigment quantity and the number of artificial statistics of yellow-leaf disease rubber in the experimental area

different colors are difficult to represent with accurate numerical values, and quantitative analysis is difficult. Because the *R*, *G*, and *B* components of the object color in the digital image are related to the amount of light shining on the object, the three components of the image obtained in the dark are very low, while the three components of the image obtained in the full sunlight are very high. Therefore, the three color components of the RGB image are actually positively correlated with the brightness, and the method of selecting the channel with the largest difference in DN value actually discards the rich information of the other two channels. Therefore, this characteristic of RGB color space is not suitable for image processing in this paper. It is necessary to find another method to extract the yellow-leaf disease region from the UAV image.

3.2 Counting accuracy regression analysis and evaluation of diseased rubber trees in HSV color space

3.2.1 Contrast enhancement

This transformation helps to enhance the contrast and highlight subtle variations in the image. By stretching the color values based on their statistical properties, decorrstretch can bring out important details in the image, making it easier to analyze and interpret (Figure 16).

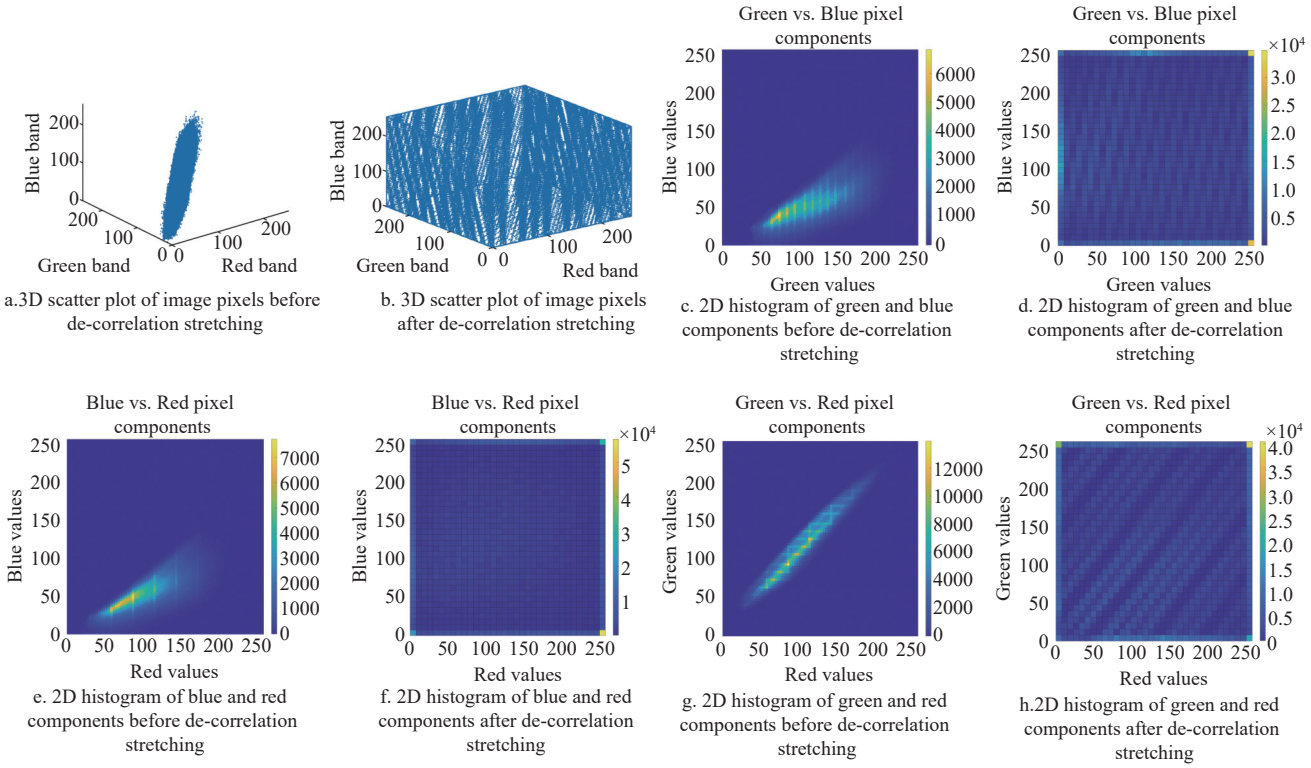

a.3D scatter plot of image pixels before de-correlation stretching

b. 3D scatter plot of image pixels after de-correlation stretching

c. 2D histogram of green and blue components before de-correlation stretching

d. 2D histogram of green and blue components after de-correlation stretching

e. 2D histogram of blue and red components before de-correlation stretching

f. 2D histogram of blue and red components after de-correlation stretching

g. 2D histogram of green and red components before de-correlation stretching

h.2D histogram of green and red components after de-correlation stretching

Figure 16 Scatter plot of image before and after decorrelation stretching.

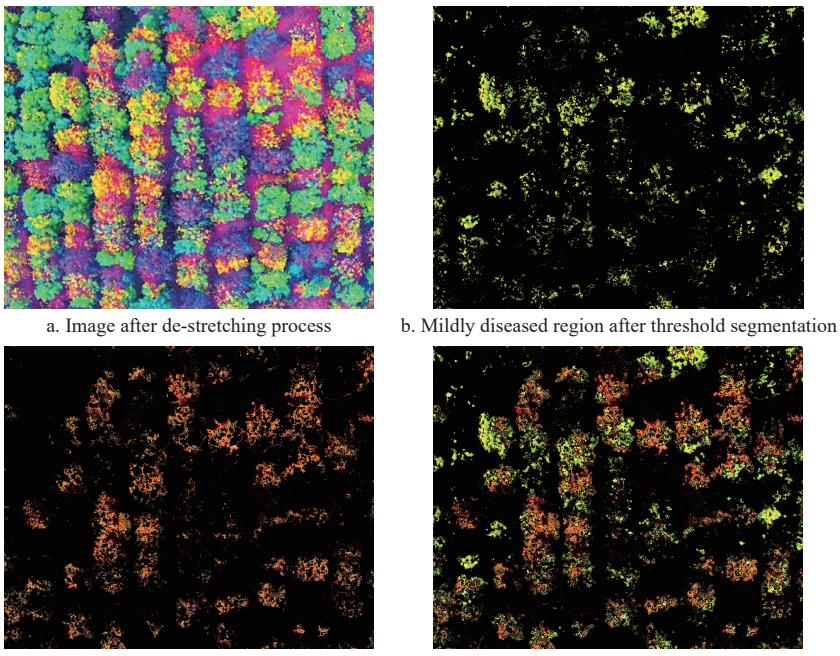

a. Image after de-stretching process

b. Mildly diseased region after threshold segmentation

c. Heavily diseased region after threshold segmentation

d. Disease area

Figure 17 Image processing step flowchart in MATLAB

We used the decorrstretch command to perform a decorrelation stretch so that the color differences in the image were expanded (Figure 17a). This study used thresholds to select yellow pixels in the range of 30-45 (V=channel 1, HSV model) and red pixels in the range of 0-20 (V=channel 1, HSV model) from the image. Yellow pixel areas corresponded to areas of mild infection, and red areas corresponded to areas of severe infection. The two were superimposed to obtain the diseased area. This provided reliable information for assessing the degree of rubber tree disease, was able to digitally count the inconspicuous yellow-leaf disease rubber trees under the drone, and also provided a basis for taking precise disease control measures (Figure 17).

3.2.2 Disease estimation based on morphological algorithms

In order to improve accuracy, the morphological algorithm was applied to fill the gap in the canopy, and the different morphological algorithm parameters were compared and analyzed (Figure 18).

As shown in Figure 19, the percentage error was the lowest at SE=5, and the median was around 5%. The 75th percentile was below 10%. In contrast, the counting performance at SE=7 was only lower than SE=5, and the counting performance at SE=3 was only better than SE=10. The percentage error in diseased rubber trees counted at SE=10 was the highest, with a median above 15%, which was caused by the large difference between actual and image processing counts of diseased rubber trees.

The percentage error is calculated as the error = (number of plants obtained by the method in this paper−actual number of diseased rubber trees)/actual number of diseased rubber trees×100%.

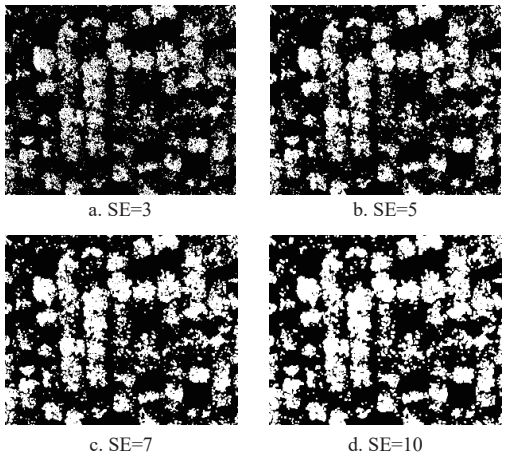

Figure 18 Filling the gap between the blades

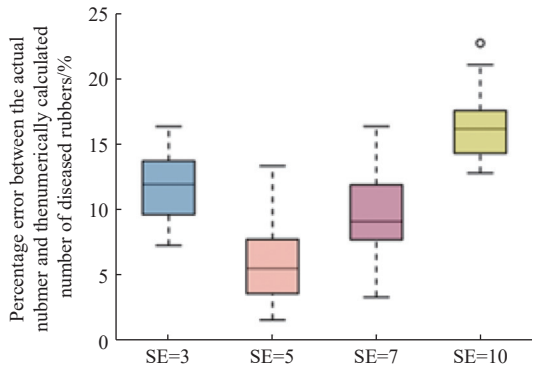

Figure 19 Box plots representing the percentage error between the actual number of rubber trees in all plots and the numerically calculated number of plants

The precise segmentation of the diseased area depends on the type of object and/or area. A clear distinction between two adjacent pixels or superpixel blocks relies on sharp color edges. Therefore, if the row spacing of rubber trees and plant spacing is larger, and there is no excessive overlap between the canopies, it will be more conducive to segmentation. If the rubber canopies are too close to each other, it will enhance the overlapping effect, which may lead to fewer counted diseased plants. Higher resolution and image clarity means sharper color edges, which means more accurate counting results than low resolution. Image clarity, flight altitude, or image sensor parameters can also affect image resolution and sharpness. Blurry images do not represent a significant error in visually and numerically distinguishing rubber trees. Figure 19 shows that when SE=5, the percentage error between the actual amount of diseased rubber trees and the amount obtained by the method in this paper was minimal. As shown in Figure 20, the R^2 of the regression model was 0.82. When SE=5, the correlation between the yellow-leaf spot rubber tree counts using the visual method as the reference method and the yellow-leaf spot rubber tree counts using the image processing method is shown in Figure 20.

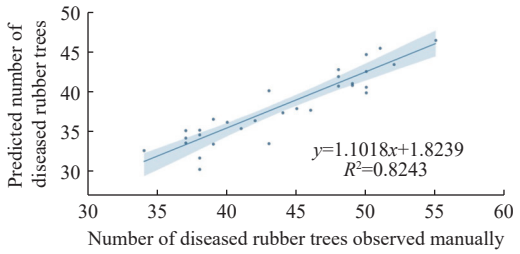

Figure 20 Performance of the method proposed in this study

The difference between artificial vision and digital counting of diseased rubber trees can be caused by a variety of factors. The uneven distribution of disease can result in overestimation or underestimation of the actual number of infected rubber trees. Another possible source of error is the presence of weeds, which have spectral reflectance similar to that of diseased areas in the visible spectrum, leading to overestimation of the number of diseased rubber trees and differences from artificial visual counting methods. In this study, after acquiring images and processing them, it was possible to create a map showing the occurrence of diseases (Figure 21).

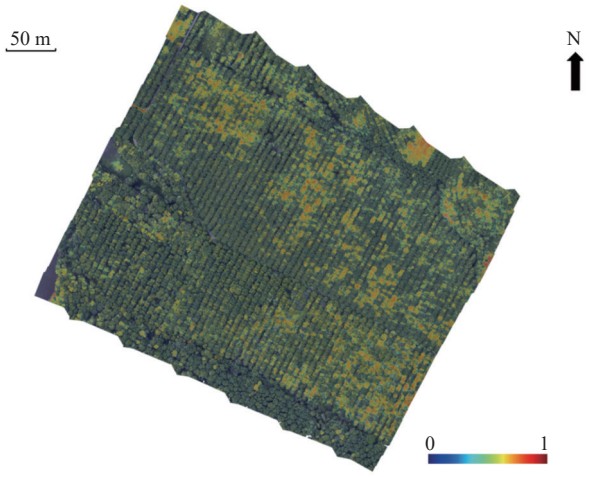

Figure 21 Rubber tree yellow-leaf disease detection map

4 Conclusions

This study proposed a method to extract the yellow-leaf disease area of the rubber tree canopy. The images were decorrelated and stretched, and the color separation between highly correlated channels was enhanced to enhance the color difference of the image. By using the "decorrstretch" command in MATLAB and combining it with a morphological algorithm, the yellow-leaf disease region in the HSV color space was able to be extracted. However, since the diseased rubber canopy in the image was sparse, there may have been errors in the counting of diseased rubber trees. To reduce these errors, this study manually selected the morphological filling parameters. This study found that when using a structuring element (SE) of 5, the percentage error between the actual number of diseased rubber trees and the number obtained by this method was the smallest. The coefficient of determination (R^2) between the number of diseased rubber trees obtained by image processing and the reference manual counting was 0.82.

In the future, rubber tree disease detection using image processing methods can be used to implement precise disease control measures and calculate potential yield forecasts.

Acknowledgements

This work was financially supported by the Young and Middle-

aged Technology Innovation and Entrepreneurship Outstanding Talents and Team Projects, Science and Technology Development Plan of Jilin Province (Grant No. 20230508032RC), and the Key Research and Development Program of Hainan Province (Grant No. ZDYF2020042). The financial support from the above funds and organizations are gratefully acknowledged.

[References]

[1] Ge J, Wang X L, Koji K. Comparing tractive performance of steel and rubber single grouser shoe under different soil moisture contents. Int J Agric & Biol Eng, 2016; 9(2): 11–20.

[2] Yoo H, Oh J, Chung W-J, Han H-W, Kim J-T, Park Y-J, et al. Measurement of stiffness and damping coefficient of rubber tractor tires using dynamic cleat test based on point contact model. Int J Agric & Biol Eng, 2021; 14(1): 157–164.

[3] Puttipipatkajorn A, Puttipipatkajorn A. Spectroscopic measurement approaches in evaluation of dry rubber content of cup lump rubber using machine learning techniques. Int J Agric & Biol Eng, 2021; 14(3): 207–213.

[4] Sabu T K, Vinod K V. Food preferences of the rubber plantation litter beetle, *Luprops tristis*, a nuisance pest in rubber tree plantations. Journal of Insect Science, 2009; 9(1): 72.

[5] Tanzini M R, Alves S B, Tamai M A, De Moraes G J, Ferla N J. An epizootic of *Calacarus heveae* (Acari: Eriophyidae) caused by *Hirsutella thompsonii* on rubber trees. Experimental & applied acarology, 2000; 24(2): 141–144.

[6] Rezende J M, Pereira J M, Araújo W S, Daud R D, Peres A J A. Population dynamics of rubber tree mites. Floresta e Ambiente, 2020; 27(4): 10.1590/2179–8087.017718.

[7] Febbiyanti T R, Kusdiana A P J. Characteristics of rhizobacteria on healthy and white rot-infected rubber trees. In: IOP Conference Series: Earth and Environmental Science. IOP Publishing, 2020; 468: 012048.

[8] Liyanage K K, Khan S, Mortimer P E, et al. Powdery mildew disease of rubber tree. Forest Pathology, 2016; 46(2): 90–103.

[9] UN FAO. Rubber tapping. Available: https://www.fao.org/4/AD221E/AD221E06.htm. Accessed on [2024-10-24].

[10] Rodrigo V H L. Adoption of different tapping systems in the rubber industry of Sri Lanka with special reference to low frequency tapping. Journal of the Rubber Research Institute of Sri Lanka, 2007; 88: 1–21.

[11] Qi D L, Zhu J L, Huang Y Q, Xie G S, Wu Z X. Factors affecting technology choice behaviour of rubber smallholders: a case study in central Hainan, China. Journal of Rubber Research, 2021; 24: 327–338.

[12] Cheng X Z, Feng Y Y, Guo A T, Huang W J, Cai Z Y, Dong Y Y, et al. Detection of rubber tree powdery mildew from leaf level hyperspectral data using continuous wavelet transform and machine learning. Remote Sensing, 2023; 16(1): 105.

[13] Kaewboonma N, Lertkrai P, Chanakot B, Lertkrai J. Thai rubber leaf disease classification using deep learning techniques. In: AICCC '23: Proceedings of the 2023 6th Artificial Intelligence and Cloud Computing Conference, 2023; pp.84-91. doi:10.1145/3639592.3639605.

[14] Li R J, Qin W B, He Y T, Li Y D, Ji R B, Wu Y H, et al. Method for the classification of tea diseases via weighted sampling and hierarchical classification learning. Int J Agric & Biol Eng, 2024; 17(3): 211–221.

[15] Yin X, Li W H, Li Z, Yi L L. Recognition of grape leaf diseases using MobileNetV3 and deep transfer learning. Int J Agric & Biol Eng, 2022; 15(3): 184–194.

[16] Liang K, Ren Z Z, Song J P, Yuan R, Zhang Q. Wheat FHB resistance assessment using hyperspectral feature band image fusion and deep learning. Int J Agric & Biol Eng, 2024; 17(2): 240–249.

[17] Eskandari R, Mahdianpari M, Mohammadimanesh F, Salehi B, Brisco B, Homayouni S. Meta-analysis of unmanned aerial vehicle (UAV) imagery for agro-environmental monitoring using machine learning and statistical models. Remote Sensing, 2020; 12(21): 3511.

[18] Olson D, Anderson J. Review on unmanned aerial vehicles, remote sensors, imagery processing, and their applications in agriculture. Agronomy Journal, 2021; 113(2): 971–992.

[19] Yang G J, Liu J G, Zhao C J, Li Z H, Huang Y B, Yu H Y, et al. Unmanned aerial vehicle remote sensing for field-based crop phenotyping: Current status and perspectives. Frontiers in Plant Science, 2017; 8: 1111.

[20] Michalska-Pożoga I, Tomkowski R, Rydzkowski T, Thakur V K. Towards the usage of image analysis technique to measure particles size and composition in wood-polymer composites. Industrial Crops and Products, 2016; 92: 149–156.

[21] Thorp K R, Dierig D A. Color image segmentation approach to monitor flowering in lesquerella. Industrial Crops and Products, 2011; 34(1): 1150–1159.

[22] Tao X Y, Li Y J, Yan W Q, Wang M J, Tan Z F, Jiang J M, et al. Heritable variation in tree growth and needle vegetation indices of slash pine (*Pinus elliottii*) using unmanned aerial vehicles (UAVs). Industrial Crops and Products, 2021; 173: 114073.

[23] Zhou D, Li M, Li Y, et al. Detection of ground straw coverage under conservation tillage based on deep learning. Computers and Electronics in Agriculture, 2020; 172: 105369.

[24] Rastogi A, Arora R, Sharma S. Leaf disease detection and grading using computer vision technology & fuzzy logic. In: 2015 2nd International Conference on Signal Processing and Integrated Networks (SPIN), Noida: IEEE, 2015; pp.500–505. doi: 10.1109/SPIN.2015.7095350.

[25] Wspanialy P, Moussa M. A detection and severity estimation system for generic diseases of tomato greenhouse plants. Computers and Electronics in Agriculture, 2020; 178: 105701.

[26] Liu L Y, Dong Y Y, Huang W J, Du X P, Ma H Q. Monitoring wheat fusarium head blight using unmanned aerial vehicle hyperspectral imagery. Remote Sensing, 2020; 12(22): 3811.

[27] Deng J, Wang R, Yang L J, Lv X, Yang Z Q, Zhang K, et al. Quantitative estimation of wheat stripe rust disease index using unmanned aerial vehicle hyperspectral imagery and innovative vegetation indices. IEEE Transactions on Geoscience and Remote Sensing, 2023; 61: 1–11.

[28] Gao A, Geng A J, Song Y P, Ren L L, Zhang Y, Han X. Detection of maize leaf diseases using improved MobileNet V3-small. Int J Agric & Biol Eng, 2023; 16(3): 225–232.

[29] Wang Y X, Xing M F, Zhang H G, He B B, Zhang Y. Rice false smut monitoring based on band selection of UAV hyperspectral data. Remote Sensing, 2023; 15(12): 2961.

[30] Li N W, Huo L N, Zhang X L. Using only the red-edge bands is sufficient to detect tree stress: A case study on the early detection of PWD using hyperspectral drone images. Computers and Electronics in Agriculture, 2024; 217: 108665.

[31] Corti M, Cavalli D, Cabassi G, et al. Application of a low-cost camera on a UAV to estimate maize nitrogen-related variables. Precision Agriculture, 2019; 20(4): 675–696.

[32] Kanning M, Kühling I, Trautz D, Jarmer T. High-resolution UAV-based hyperspectral imagery for LAI and chlorophyll estimations from wheat for yield prediction. Remote Sensing, 2018; 10(12): 2000.

[33] Wang S W, Niu Y X, Ma X Y, Chen S L, Amani, Feng H. Prediction model for nitrogen content of rice leaves during heading stage in cold region based on hyperspectrum. Journal of Agricultural Mechanization Research, 2019; 41(3): 158–164. (in Chinese)

[34] Mazlan S, JAAFAR N M, Wahab A, Sulaiman Z. Major diseases of rubber (*Hevea brasiliensis*) in Malaysia. Pertanika Journal of Scholarly Research Reviews, 2019; 5(2): 10–21.

[35] Hamid N R A, Ghani Z A, Mahsuri I, Yusoff M A M, Rasib, A W, Yusoff A R M, et al. Rubber leaf disease detection from low altitude remote sensing techniques. Advanced Science Letters, 2018; 24(6): 4281–4285.

[36] Tang C R, Yeng M, Fang Y J, Luo Y F, Gao S H, Xiao X H, et al. The rubber tree genome reveals new insights into rubber production and species adaptation. Nature Plants, 2016; 2: 16073.

[37] Cheng H, Tang C, Huang H. The Reyan 7-33-97 rubber tree genome: insight into its structure, composition and application. The Rubber Tree Genome, 2020: 13–40.

[38] Achanta R, Shaji A, Smith K, Lucchi A, Fua P, Susstrunk S. SLIC superpixels compared to state-of-the-art superpixel methods. IEEE Transactions on Pattern Analysis and Machine Intelligence, 2012; 34(11): 2274–2282.

[39] Swain M J, Ballard D H. Color indexing international journal of computer vision, 1991; 7(1): 11–32.

[40] Lu S Y, Wang B Z. An image retrieval algorithm based on improved color histogram. In: Journal of Physics: Conference Series. IOP Publishing, 2019; 1176(2): 022039.

[41] Lee H S, In Cho S. Spatial color histogram-based image segmentation using texture-aware region merging. Multimedia Tools and Applications, 2022; 81(17): 24573–24600.